Enhancing Sustainable Energy Conversion Efficiency by Incorporating Photoelectric Responsiveness into Multiporous Ionic Membrane

Weipeng Xian, Changjia Zhu, Zhuozhi Lai, Xiuhui Zuo, Qing-Wei Meng, Liping Zheng, Sai Wang, Zhifeng Dai, Fang Chen, Shengqian Ma,* and Qi Sun*

The evolution of porous membranes has revitalized their potential application in sustainable osmotic-energy conversion. However, the performance of multiporous membranes deviates significantly from the linear extrapolation of single-pore membranes, primarily due to the occurrence of ion-concentration polarization (ICP). This study proposes a robust strategy to overcome this challenge by incorporating photoelectric responsiveness into permselective membranes. By introducing light-induced electric fields within the membrane, the transport of ions is accelerated, leading to a reduction in the diffusion boundary layer and effectively mitigating the detrimental effects of ICP. The developed photoelectric-responsive covalent-organic-framework membranes exhibit an impressive output power density of 69.6 W m^{-2} under illumination, surpassing the commercial viability threshold by $\approx$14-fold. This research uncovers a previously unexplored benefit of integrating optical electric conversion with reverse electrodialysis, thereby enhancing energy conversion efficiency.

1. Introduction

Blue energy, also known as osmotic power, capitalizes on the energy potential derived from the discrepancy in the Gibbs free energies between seawater and river water. The resulting energy can be substantial, with peaks of up to 2.3 MJ per cubic meter of water.[1–4] Among the techniques being explored to harness this energy, reverse electrodialysis (RED) has emerged as one of the most promising, as it allows for the direct conversion of salinity gradients into electricity by facilitating the directional movement of charges through permselective membranes.[5–15] However, there is a challenge when it comes to scaling up this process efficiently. Membranes with a single pore can generate high power densities, but the issue lies in replicating this performance on a larger scale.[16–18] One primary obstacle is ion-concentration polarization (ICP), a phenomenon that becomes more noticeable in highly porous membranes. In these membranes, a depletion zone forms at one pore entrance, while an area of increased ionic concentration appears at the opposite entrance, creating a diffusion boundary layer (**Figure 1a**). This disruption compromises the concentration gradient required for efficient energy extraction. Despite advancements made in nanoporous membranes, their performance in practical applications still falls short, which restricts their broader use.[19–21] Therefore, addressing the ICP phenomenon should be a priority for enhancing the efficiency of the RED process in generating blue energy.

In previous studies, we have demonstrated that a temperature gradient between saline solutions has the potential to alleviate ICP. By introducing an additional ion-driving force, the

W. Xian, Z. Lai, X. Zuo, Q.-W. Meng, S. Wang, Q. Sun
Zhejiang Provincial Key Laboratory of Advanced Chemical Engineering
Manufacture Technology
College of Chemical and Biological Engineering
Zhejiang University
Hangzhou 310027, China
E-mail: sunqichs@zju.edu.cn
C. Zhu, S. Ma
Department of Chemistry
University of North Texas
1508 W Mulberry, St Denton, TX 76201, USA
E-mail: shengqian.ma@unt.edu.cn

L. Zheng, Z. Dai
Key Laboratory of Surface & Interface Science of Polymer Materials of
Zhejiang Province
Zhejiang Sci-Tech University
Hangzhou 310028, China
F. Chen
Department of Chemistry
Zhejiang University
Hangzhou 310028, China
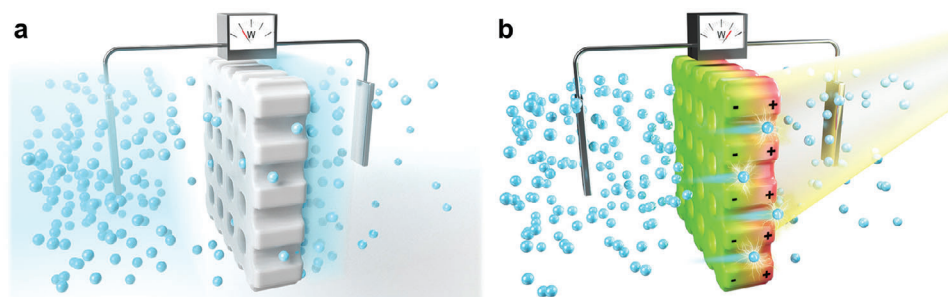
Figure 1. Conceptual diagram. a) Illustration depicting the ion-concentration polarization (ICP) phenomenon with an ionic membrane. The boundary layer adjacent to the membrane surface on the side with higher ion concentration experiences a decrease in target ion concentration, while the side with lower ion concentration experiences an increase. b) Proposed strategy to mitigate ICP by utilizing photoelectric-responsive ionic membranes. These membranes generate a built-in electric field when exposed to light, facilitating directed ion transport.

diffusion boundary layer can be reduced, leading to an increase in the effective concentration gradient.[22,23] However, the results obtained by integrating thermoelectric conversion with RED are not directly applicable to practical operating conditions that involve a large volume of water. To utilize nanoporous membranes for osmotic energy harvesting in real-world scenarios, it is vital to develop alternative methods for alleviating ICP without compromising porosity and charge density. Among the various external stimuli, light emerges as an attractive option, as it is ubiquitous, noninvasive, and environmentally friendly. It can directly interact with the membrane, significantly enhancing efficiency as well as providing the opportunity for temporal and spatial control.[24–39] Moreover, light energy can create an electrochemical gradient across a membrane with a photo-electric response; this may provide an alternative strategy to alleviate ICP by utilizing the built-in electric field to mitigate ICP (Figure 1b).

To explore the validity of the above-mentioned hypothesis, our study focused on covalent organic frameworks (COFs). The unmatched versatility of COFs in terms of geometry and surface properties enables the use of chromophores as building blocks and allows for the straightforward grafting of ionic moieties along the pore walls; this ensures a feasible conceptual leap for the synthesis of ionic photoelectric-responsive materials.[40–49] Additionally, the utilization of 2D COFs (2D COFs) offers unparalleled advantages in membrane construction. The arrangement of conjugated 2D sheets in stacked configurations promotes the migration of charge carriers, while the continuous 1D channels created provide paths for ion transport.[50–58] In this study, we designed and developed a set of 2D porphyrin-based ionic COF membranes. Upon light illumination, these membranes undergo effective separation of charge carriers, resulting in the generation of a transmembrane electric field that drives directional ion transport. This light-induced process significantly alleviates ICP, showing a decreased ion diffusion boundary layer. Notably, when exposed to simulated sunlight, our RED device yielded an impressive output power density of 69.6 ± 1.3 W m^{-2}, positioning it as one of the most promising options available for practical applications (Table S1, Supporting Information). Consequently, our findings offer a perspective on enhancing the energy conversion efficiency of RED systems.

2. Results and Discussion

2.1. Membrane Preparation and Characterization

Freestanding porphyrin-based COF membranes were fabricated via an acetic acid-catalyzed Schiff base condensation reaction under liquid-liquid interfacial polymerization conditions. This involved combining an aqueous acetic acid solution of 4,4′,4″,4‴-(porphyrin-5,10,15,20-tetrayl)tetraaniline (PTA) with an ethyl acetate-mesitylene ditopic aldehyde solution. To optimize the density of ionic sites, and consequently, the accompanying permselectivity, we employed a multivariate (MTV) strategy to control the distribution of the reactive sites.[59,60] Specifically, various ratios of 2,5-dihydroxyterephthaldeyde (DHA) and 2,5-dimethoxyterephthaldeyde (DMA) were paired with PTA, followed by treatment with 2,3-epoxypropyltrimethylammonium chloride to introduce cationic sites via a ring-opening reaction between the hydroxyl groups on DHA and epoxy groups, with the resulting membranes denoted as COF-DMA$_x$DHA$_y$ and COF-DMA$_x$DHA$_y$-QA, respectively (x and y represent the molar ratios of DMA and DHA of the as-synthesized membranes, respectively; **Figure 2a**). The local chemical structures of the membranes were characterized by solid-state ^{13}C nuclear magnetic resonance spectroscopy (^{13}C NMR) and Fourier-transform infrared spectroscopy (FT-IR). The NMR signal at 162.2 ppm, attributed to $C = N$ of the imine group, indicates the formation of COFs.[61] The FT-IR spectra of the COF-DMA$_x$DHA$_y$ membranes showed a characteristic peak at 1612 cm^{-1}, representing the stretching vibration of the $C = N$ bond in the imine group. Notably, the peaks associated with the NH$_2$ and CHO groups of the monomers at 3210–3335 and 1670 cm^{-1}, respectively, almost disappeared, indicating a high degree of membrane polymerization (Figures S1 and S2, Supporting Information).[62] Scanning electron microscopy (SEM) images of the COF-DMA$_x$DHA$_y$ membranes revealed a smooth surface with no visible defects, implying that ions could pass exclusively through the inherent COF pores (Figure 2b). The cross-sectional SEM images displayed a densely packed structure measuring ≈500 nm in thickness (Figures S3–S6, Supporting Information). High-resolution transmission electron microscopy (HR-TEM) images demonstrated that the membrane exhibited high crystallinity, with a tetragonal

**ADVANCED
SCIENCE NEWS**

www.advancedsciencenews.com

NANO · MICRO

small

www.small-journal.com
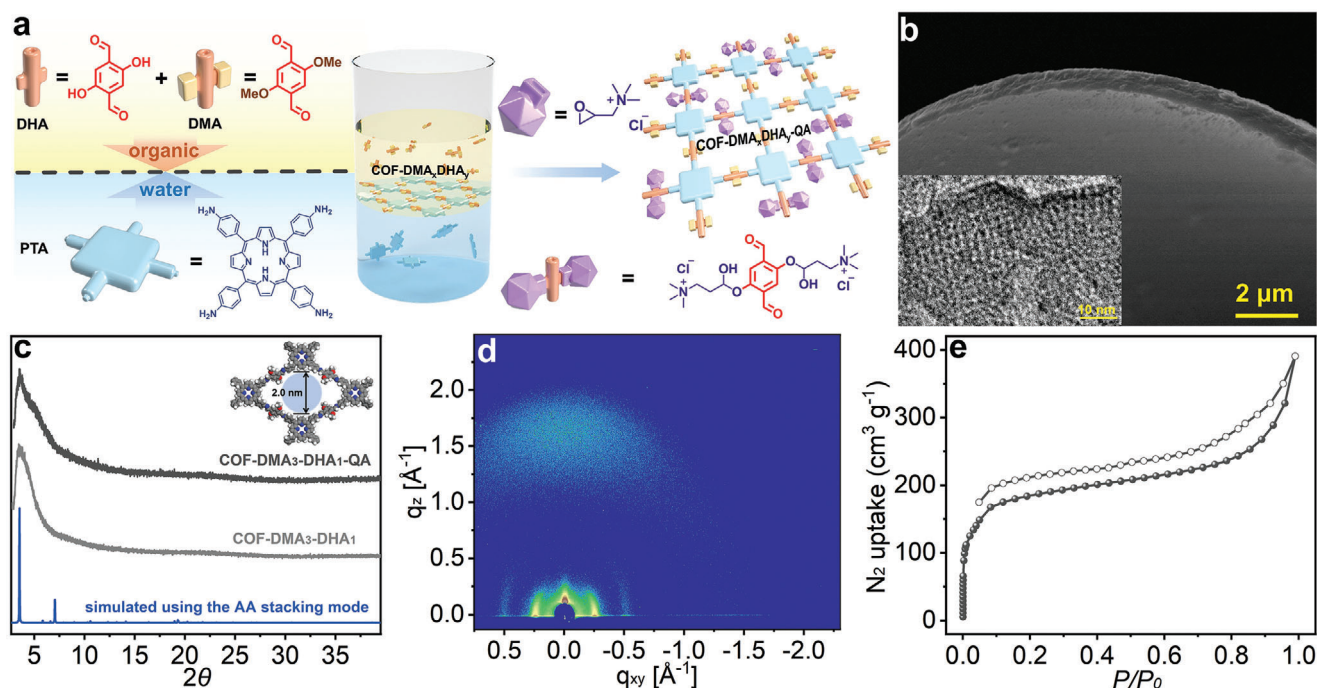
Figure 2. Membrane synthesis and characterization. a) Synthesis scheme depicting the fabrication of freestanding COF-DMA$_x$DHA$_y$ membranes via interfacial polymerization, followed by post-synthetic modification with 2,3-epoxypropyltrimethylammonium chloride to yield COF-DMA$_x$DHA$_y$-QA. A MTV strategy was employed to regulate the distribution of reactive sites. b) Representative SEM image (inset, TEM image), c) XRD patterns (inset, graphical view of AA stacking structure), d) GIWAXS pattern, and e) N$_2$ sorption isotherms collected at 77 K of the COF-DMA$_3$DHA$_1$ membrane.

pore size of ≈2.0 nm (inset of Figure 2b; Figure S7, Supporting Information). Analysis of the powder X-ray diffraction (PXRD) patterns of the freestanding membranes revealed a set of sharp reflections with mirrored positions, confirming the formation of highly crystalline materials and the preservation of the underlying topology of the COF using the MTV strategy (Figure 2c; Figure S8, Supporting Information). To validate the structure, experimental data was compared to a simulated pattern of the PBAN arrangement, which revealed a pore size of 2.0 nm along the c-axis, consistent with the TEM results (Figure 2c, inset). Additionally, 2D grazing-incidence wide-angle X-ray scattering (GI-WAXS) measurements provided further evidence of the textured nature of the freestanding membranes. The hk0 reflections of COF-DMA$_3$DHA$_1$ exhibited the highest intensity near the sample horizon, highlighting the preferred orientation of the a-b plane (Figure 2d). This orientation is particularly desirable as it ensures full accessibility of the COF pores, which align parallel to the transport pathway.[63] The Brunauer–Emmett–Teller (BET) surface area of COF-DMA$_3$DHA$_1$, calculated using the nitrogen sorption isotherms, was 578 m^2 g^{-1}, with a pore size distribution centered at 2.4 nm (Figure 2e; Figure S9, Supporting Information).

Subsequently, SEM, PXRD, X-ray photoelectron spectroscopy (XPS), FT-IR, and solid-state ^{13}C NMR analyses were performed to examine the post-synthetic modifications. The SEM images demonstrated that the membranes maintained their original morphology after chemical treatment with 2,3-epoxypropyltrimethylammonium chloride (Figures S10–S13, Supporting Information). Comparison of the PXRD patterns between COF-DMA$_x$DHA$_y$-QA and COF-DMA$_x$DHA$_y$ confirmed

the preservation of crystallinity after the post-synthetic modification (Figure S14, Supporting Information). The appearance of chloride signals (Cl 2p at 199.9 eV) in the XPS profiles of the COF-DMA$_x$DHA$_y$-QA membranes confirmed the occurrence of chemical transformations (Figure S15, Supporting Information). Additional peaks at 1487 and 1035 cm^{-1} in the FT-IR spectra of the COF-DMA$_x$DHA$_y$-QA membranes were attributed to C-C and C-N stretching vibrations, respectively, indicating the incorporation of quaternary ammonium groups (Figure S16, Supporting Information). This was confirmed by solid-state ^{13}C NMR spectra (Figure S17, Supporting Information). In the XPS profiles of COF-DMA$_x$DHA$_y$-QA, the N 1s peak was deconvoluted into three peaks at 398.5, 399.4, and 402.3 eV, corresponding to imine bonds, porphyrin rings, and quaternary ammonium groups, respectively.[64] This allowed for quantification of the content of the ionic sites on COF-DMA$_x$DHA$_y$-QA. Based on the framework structures, the integral area ratios of the N species from the imine groups and porphyrin rings in these materials are ≈2. Therefore, the estimated contents of the ionic sites in the membranes were 0.15, 0.39, 0.62, and 0.77 mmol g^{-1} for COF-DMA$_9$DHA$_1$-QA, COF-DMA$_3$DHA$_1$-QA, COF-DMA$_1$DHA$_1$-QA, and COF-DMA$_1$DHA$_3$-QA, respectively (Figure S18, Supporting Information). We performed UV–Vis spectroscopy to evaluate the light-absorption characteristics of the membranes, which displayed significant absorbance across the UV–Vis spectrum. The Tauc plot analysis allowed us to estimate the optical bandgap as 2.94 and 2.84 eV for COF-DMA$_3$DHA$_1$ and COF-DMA$_3$DHA$_1$-QA, respectively (Figure S19, Supporting Information). The presence of a direct visible-range bandgap makes these membranes attractive for optoelectronic applications.
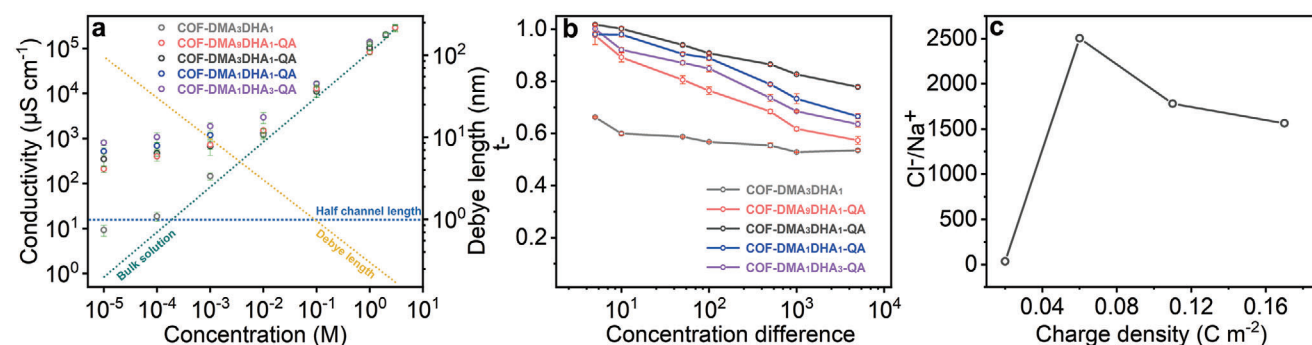
Figure 3. Investigation of ionic-transport properties of COF-DMA$_x$DHA$_y$-QA. a) Surface-charge-governed ion transport. The plot shows the variation in conductivity with KCl concentration for COF-DMA$_x$DHA$_y$-QA. The half-channel length denotes the radius of the membrane pore channels. At solution concentrations below the point where half the channel length intersects with the Debye length, the electrical double layer extends into and overlaps with the channel. b) The t_- plots against different KCl concentration differences across COF-DMA$_x$DHA$_y$-QA. The error bars indicate the standard deviation from three independent measurements of the membranes. c) COMSOL simulation. The impact of charge densities on the Cl$^-$/Na$^+$ ratio at the mouth of the low-concentration side (blue dashed line shown in Figure S22, Supporting Information) for the channels with different charge densities.

2.2. Investigation of Ionic-Transport Properties of COF-DMAxDHAy-QA
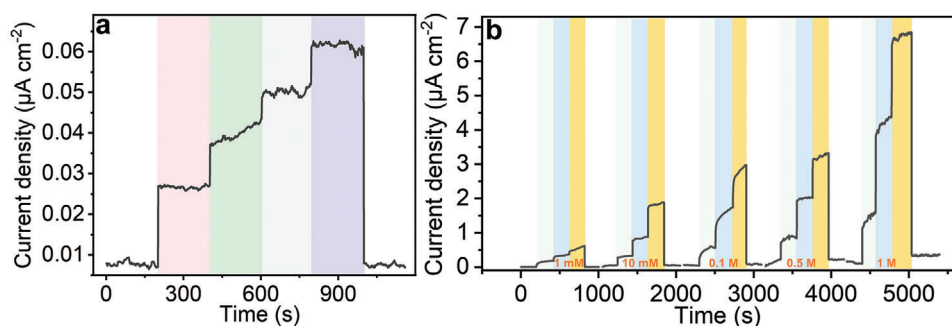
To assess the compactness of the membrane, we investigated the transmembrane ion behavior under symmetrical KCl solutions by fitting the current-voltage (I-V) curves to the conductance model. Analysis of the normalized conductivity versus the concentration of aqueous KCl solution revealed a significant deviation of transmembrane conductance from the bulk value (represented by the dashed line) at KCl concentrations below 0.1 M. This indicates that at these conditions, the electrical double layers (EDLs) overlap the pore channels, leading to ion transport governed by surface charge.[65] Remarkably, as the density of ionic sites increases, the transmembrane conductance values in this range also increase. This phenomenon arises because the ionic conductivity of a nanochannel primarily relies on the accumulated counterions, which are determined by the density of the surface charge. Upon further increasing the KCl concentration, the transmembrane conductance approaches the bulk value, indicating that the thickness of the EDL at these concentrations becomes smaller than the radius of the pore channels. As a result, the surface-charge-governed ion transport weakens (**Figure 3a**). By considering the relationship between the electrolyte concentration and the Debye length, we estimated the pore sizes of these membranes to be ≈2 nm, aligning excellently with the COF structure (Table S2, Supporting Information).

Given that the conversion of ionic energy into electrical energy relies solely on charge separation, we evaluated the permselectivity of COF-DMA$_x$DHA$_y$-QA by measuring the open-circuit voltage (V_{oc}) across the membranes at various KCl concentrations. To confirm the effect of the introduced ionic sites, we compared the permselectivities of COF-DMA$_3$DHA$_1$ and COF-DMA$_3$DHA$_1$-QA. Analysis of the anion transference numbers (t_-) plotted against concentration differences revealed that COF-DMA$_3$DHA$_1$ showed minimal anion selectivity, with values below 0.6 for concentration differences exceeding 10. However, the inclusion of positive quaternary ammonium groups significantly enhanced the permselectivity. Even at a concentration difference of 1000, the values remained at 0.83 (Figure 3b). It should be noted that increasing or decreasing the number of ionic sites

on the membrane beyond a certain range negatively affected the permselectivity (Figures S20 and S21, Supporting Information). This phenomenon can be explained by the tradeoff between charge selectivity and the degree of ICP. A charge density that is too low fails to induce a strongly overlapping EDL, whereas excessive charge density leads to severe ICP, thereby compromising the ion-screening ability.[66] The validity of this assumption was further supported by a COMSOL simulation that determined the concentration ratio of anions and cations near the channel aperture. The simulation indicated that COF-DMA$_3$DHA$_1$, with a charge density of 0.06 C m^{-2}, exhibited the optimal permselectivity among the tested membranes (Figure 3c; Figure S22, and Table S3, Supporting Information).

2.3. Investigation of Light-Responsive Transmembrane Ion Transport

COF-DMA$_3$DHA$_1$-QA, which exhibited excellent permselectivity, was selected as the membrane for investigating light-modulated ionic transport. The membranes were securely clamped between two quartz compartments, both filled with identical KCl solutions spanning concentrations from 1 mM to 1 M. To evaluate the photoelectrical properties of the device, current–time (I–t) traces were recorded under alternating light-on and light-off conditions using a pair of Ag/AgCl electrodes. In the absence of light, the system reached a steady state, with a small amount of electrons flowing through the external circuit due to the unequal diffusion coefficients of K$^+$ and Cl$^-$ ions, resulting in the creation of a transmembrane potential.[67] Upon light irradiation, an instantaneous photoelectric response was observed and captured in the I–t trace. This response remained stable throughout the period of irradiation. For instance, using a blue LED lamp with an intensity of 5 mW cm^{-2} led to an increase in current density by 0.05 ± 0.01 µA cm^{-2}. Notably, the intensity of the light-induced ionic current varied depending on the wavelength of light. The order of response was blue ≈ white > green > red LED lamp (**Figure 4a**). This trend matches the maximum absorption wavelength seen in the UV–Vis spectrum of the COF-DMA$_3$DHA$_1$-QA membrane. To mimic natural sunlight, Xe lamps were employed

**ADVANCED
SCIENCE NEWS**

www.advancedsciencenews.com

NANO · MICRO

small

www.small-journal.com

Figure 4. Investigation of light-trigged ionic responses of COF-DMA$_3$DHA$_1$-QA. a) I–t curves of the device measured in the dark and upon light illumination, using various LED lamps (red, green, gray, and blue backgrounds represent red, green, white, and blue light, respectively). The two compartments were filled with 1 mM aqueous KCl solutions. b) I–t traces recorded under illumination with various intensities of xenon lamp (light green, light blue, and orange backgrounds represent 20, 40, and 100 mW cm^{-2} xenon lamp, respectively). The measurements were conducted with different equimolar concentrations of aqueous KCl solutions ranging from 1 mM to 1 M.

in subsequent tests. The results revealed a significant correlation between the amplitude of the photocurrent generated and both the light intensity and KCl concentration. The light-induced ion current density exhibits a gradual increase with the escalation of both light intensity and KCl concentration (Figure S24, Supporting Information). Impressively, when exposed to a 100 mW cm^{-2} Xe lamp, a peak photocurrent density of 6.8 ± 0.3 μA cm^{-2} was reached with 1 M KCl, having an on-off ratio of 46 (Figure 4b). It is worth highlighting that COF-DMA$_3$DHA$_1$-QA exhibited a superior light response compared to its unmodified counterpart (COF-DMA$_3$DHA$_1$), with a maximum ratio difference of 2.2 (Figures S23 and S25, Supporting Information). This enhanced light response can be attributed to the higher ionic conductivity of COF-DMA$_3$DHA$_1$-QA after the introduction of ionic sites compared to COF-DMA$_3$DHA$_1$.

Next, a set of control experiments were performed to elucidate the origin of the observed photogate effects. The possibility that the observed light responsivity was the result of a light-induced electrode reaction was initially ruled out. This was done by evaluating the light responsivity of a transparent polyacrylonitrile (PAN) membrane, having a molecular weight cut-off of 50,000 Da. The resulting magnitude of photocurrent was found to be less than one-tenth of that produced using COF-DMA$_3$DHA$_1$-QA (Figure S26, Supporting Information). Following this, the potential impact of a light-activated temperature gradient between two compartments was explored. Measurements during testing showed a maximum temperature difference of 3.5 K between the

solutions. A synchronously observed current increment (ΔI) in response to temperature changes in 0.5 M KCl indicated that a 3.5 K temperature gradient leads to an approximate current increment of 0.04 ± 0.002 μA cm^{-2} (**Figure 5a**). This value is ≈80 times smaller than the photocurrent obtained upon light exposure (3.3 ± 0.1 μA cm^{-2}). Furthermore, the photothermal effect of the illumination could potentially cause a temperature rise in the membrane. In fact, the temperature of the illuminated membrane rose by ≈4.9 K (Figure S27, Supporting Information). However, this light-induced increase in membrane temperature can be disregarded in this context, as the axial temperature gradient would provoke ion transport in a direction opposed to the observed photocurrent. As a result, the temperature gradient induced by light doesn't have a major influence on the detected current response.

Experiments were further conducted to investigate the underlying mechanism behind the observed photogating effects. In order to determine the direction of the photoionic effect, the experiments were performed under gradient conditions. A conductive cell consisting of three compartments was used for this purpose. The compartments were sequentially filled with 10^{-6} and 5 × 10^{-5} M aqueous KCl solutions (Figure S28, Supporting Information). To eliminate the redox potential of Ag/AgCl caused by uneven potential drop at the electrode-electrolyte interface, a pair of Ag/AgCl electrodes was inserted into the side compartments containing identical KCl solutions. To prevent rapid mixing of the solutions, a non-selective PAN membrane
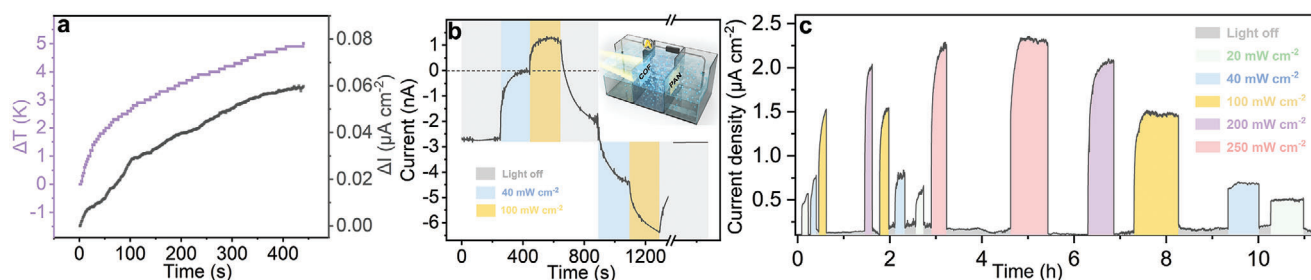
Figure 5. Investigation of the origin of light-trigged directional ion transport in COF-DMA$_3$DHA$_1$-QA. a) Synchronous time evolution of the ΔI in relation to the temperature difference across the KCl aqueous solutions segregated by the membrane. b) Changes in current in response to various external stimuli. c) Reversibility of photocurrent. A two-compartment cell filled with symmetric 10 mM aqueous KCl solutions was employed.
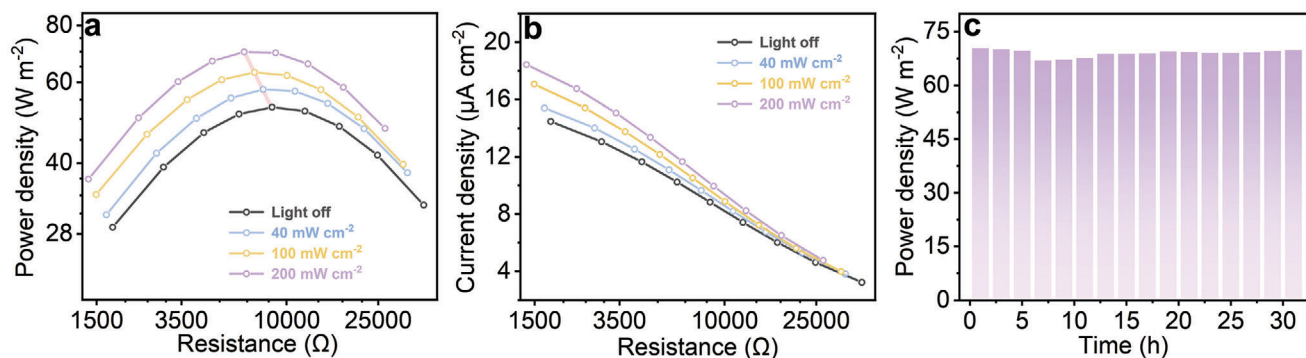
Figure 6. Output power density of the RED device assembled using COF-DMA$_3$DHA$_1$-QA and Nafion 212. a) Power output to an external circuit to supply an electronic load before and after illumination under 40, 100, or 200 mW cm^{-2} xenon lamp. b) The corresponding variation of diffusion current. c) Time series of the power density of the RED device by mixing 0.01/0.5 M NaCl illuminated under 200 mW cm^{-2} xenon lamp.
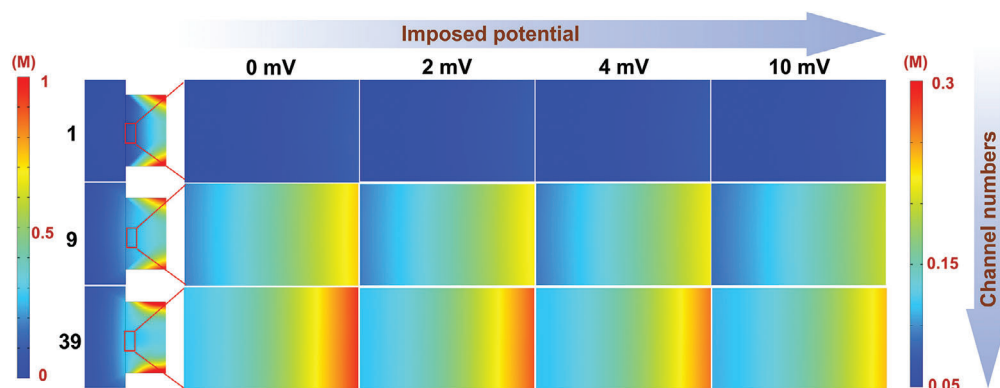
was used in combination with COF-DMA$_3$DHA$_1$-QA. Initially, a diffusion current driven by the concentration gradient was observed, with a magnitude of ≈-2.7 nA. However, when the membrane was illuminated with a light intensity of 40 mW cm^{-2} from the high-concentration side, the photo-driven ion transport counteracted the diffusion due to the concentration gradient. As a result, the current value increased from -2.7 nA to ≈0 nA. Interestingly, when the light power density was further increased to 100 mW cm^{-2}, a remarkable phenomenon occurred. The ionic current crossed the zero line and immediately reversed its direction, increasing in the opposite direction to its initial value of 1.3 nA. It is worth noting that when the membrane facing the low-concentration side was exposed to light, the current became more negative with an absolute value that intensified with the increase in light intensity (Figure 5b). These variations in the current clearly indicate that the directionality of the light-induced membrane potential is opposite to the potential difference induced by the concentration gradient. This observation is similar to what is observed in biological light-driven ion pumps, where light energy is converted into electronically excited energy to generate a net membrane potential that drives ions in the direction opposite to that of the electrochemical gradient. To support our interpretation, we performed photocurrent experiments with and without an external voltage. Figure S29 (Supporting Information) illustrates that the generated photocurrent counterbalanced the voltage-driven ionic current, indicating that the light-induced transmembrane potential served as the driving force for ion migration. When light interacts with the COF membrane, it excites the ground-state electrons, leading to the establishment of a membrane potential between the illuminated and unilluminated sides. With the increasing power density of light, photochemical reactions become more pronounced, resulting in the generation of charge-separated species and a higher transmembrane potential. Consequently, a greater photoinduced ionic current is observed (Figure S30, Supporting Information). Furthermore, the presence of a photovoltage and photocurrent during light exposure, which rapidly vanish upon cessation of light, indicates the generation and fast recombination of light-triggered excitons. This observation is consistent with the experimental results obtained when testing the reversibility of the photogate phenomenon between dark and illuminated states at varying intensities of the Xe lamp. The responses demonstrated full reversibil-

ity, with the photocurrents diminishing immediately upon light cessation and returning to a transport regime comparable to that observed in the dark reference experiment (Figure 5c). The light-induced formation of an electrostatic potential across the membrane was confirmed through the surface photovoltage spectrum. Upon irradiation with 400 nm light, an approximate increment of 10 mV was observed (Figure S31, Supporting Information).

2.4. Evaluation of Osmotic Energy Conversion

The remarkable permselectivity and light responsivity exhibited by COF-DMA$_3$DHA$_1$-QA have sparked interest in exploring its potential of mitigating ICP in osmotic energy conversion. In traditional RED devices, salinity gradient energy is harnessed by utilizing alternating anionic and cationic membranes. To align with this approach, we paired COF-DMA$_3$DHA$_1$-QA with the cation-selective membrane Nafion 212, as depicted in Figure S32 (Supporting Information). A three-compartment conductivity cell was used to simulate estuarine conditions by alternating the filling of compartments with NaCl solutions of 0.01 M and 0.5 M. During the process, the power generated was extracted using an external load resistor (R_L). Analysis of the data presented in **Figure 6a,b** revealed that the diffusion current gradually decreased as the R_L value increased. The maximum output power density was achieved at an R_L value of 6.5 kΩ. By employing the equation $P_{out} = I^2 R_L$, where I represents current density, we estimated the maximum output power density to be 53.2 ± 0.9 W m^{-2} (Figure S33, Supporting Information). For comparison, under otherwise identical conditions, the COF-DMA$_3$DHA$_1$ membrane yielded an output power density of 18.9 ± 1.1 W m^{-2}, emphasizing the significant impact of the introduced ionic sites (Figure S34, Supporting Information).

Based on the opto-ionic effects mentioned earlier, it was expected that light would synergistically enhance ion permeability and increase the output power density of this RED device. Indeed, when exposed to light irradiation, there were enhancements in both the V_{oc} and short-circuit current (I_{sc}). Specifically, the values increased from 123.1 mV and 13.6 µA to 126.9 mV and 17.2 µA, respectively, upon illumination with 200 mW cm^{-2} of light. Consequently, the calculated power density reached 69.6 ± 1.3 W m^{-2}, representing a 30% increase compared to the value achieved in

ADVANCED
SCIENCE NEWS

www.advancedsciencenews.com

NANO · MICRO
small
www.small-journal.com

Figure 7. COMSOL simulations. Impacts of channel densities and imposed voltages on the distribution of Cl⁻ ions near the aperture facing the low concentration side.

the absence of light (Figure 6a,b, Figures S33 and S35, Supporting Information). However, in the presence of 0.5 M NaCl and under light irradiation (Figure S36, Supporting Information), the power density was only 0.1 W m⁻². These observations suggest a synergistic effect of the salinity gradient and light irradiation on the conversion of ionic energy. Furthermore, the average amplitudes of the current and transmembrane potentials remained consistent during light conditions for a minimum of 15 cycles, demonstrating operational stability (Figure 6c).

To gain a deeper understanding of this intriguing phenomenon at the molecular level, we performed COMSOL simulation. To facilitate the calculations, 2D models incorporating channels measuring 220 nm in length and 2 nm in diameter were developed (Figure S37 and Table S4, Supporting Information). A charge density of 0.06 C m⁻², in accordance with the charge density of COF-DMA$_3$DHA$_1$-QA, was uniformly imposed throughout the pore channel. We then analyzed the variations in ion distribution resulting from the mixing of 0.01 and 0.5 M NaCl solutions as the number of channels increased. Despite a consistent ionic concentration across the channels with an increase in channel number, distinct differences in the concentration of Cl⁻ ions at the end of the channels were observed (Figure S38, Supporting Information). Notably, the Cl⁻ concentration near the channel mouth facing the 0.5 M NaCl solution was lower compared to the bulk solution. On the other hand, it was higher in the reservoir containing 0.01 M NaCl, leading to a diminished effective driving force—this phenomenon is referred to as ICP (**Figure 7**; Figure S39, Supporting Information).

We conducted a comprehensive analysis comparing the Cl⁻ concentration profiles in systems with varying numbers of channels. Our findings showed that the deviations in local concentration were more pronounced at the low-concentration ends than at the high-concentration ends. Notably, this deviation was most significant in the system comprising 39 channels, which had a pore density aligned with that of the membrane. In this configuration, the localized Cl⁻ concentration near the channels could reach ≈20 times higher than the average value, resulting in disruptions to the concentration gradient across the membrane. Specifically, the Cl⁻ concentration ratio at the ends of the channels, facing the high- and low-concentration sides $(C(Cl^-)_H/C(Cl^-)_L)$, decreased from 17.3 in the single-channel system to 5.5 in the 39-channel

system. To investigate the impact of the transmembrane potential generated by the photoelectrical effect on ion distribution, we imposed a potential across the system. Our simulations revealed that when a transmembrane potential of 2 mV was applied, the $(C(Cl^-)_H/C(Cl^-)_L)$ ratio in the 39-channel system increased from 5.5 to 5.8. A more pronounced effect was observed with a further increase in potential to 10 mV, as determined through the surface photovoltage spectrum, which resulted in a $(C(Cl^-)_H/C(Cl^-)_L)$ ratio of seven, indicating a reduction in ICP (Table S5, Supporting Information). Notably, the simulated increment in the concentration gradient (27.3%) corresponded well with the increment in the output power density (30.8%).

3. Conclusion

In summary, our study provides compelling evidence that harnessing the transmembrane electric field generated through the photoelectric effect in multi-pore membranes offers an effective solution to the inherent challenges of ICP in RED systems. By further refining the material design to enhance the photoelectrical effect, it is conceivable that the impact of ICP can be further mitigated. The ubiquity of light makes it a highly attractive resource for enhancing the functionality of membranes. These advancements hold great promise across diverse fields, ranging from energy conversion and artificial photosynthesis to smart separation techniques. Our research serves as a foundation for deeper exploration of light-augmented methods in membrane technology, thereby opening up opportunities for enhanced energy efficiency and the resolution of critical environmental issues.

4. Experimental Section

Commercially available reagents were purchased in high purity and used without purification. The synthesis procedures for the membranes were described in detail in the Material Synthesis section of the Supporting Information. The asymmetric polyacrylonitrile (PAN) ultrafiltration membrane with a molecular weight cut-off of 50,000 Da was sourced from Sepro Membranes Inc. (Carlsbad, CA, USA). Nafion 212 was obtained from DuPont (Wilmington, DE, USA) with a thickness of 50 μm.

X-ray powder diffraction (XRD) patterns were obtained using a Rigaku Ultimate VI X-ray diffractometer operating at 40 kV and 40 mA, with CuKα

**ADVANCED
SCIENCE NEWS**

www.advancedsciencenews.com

**NANO · MICRO
small**

www.small-journal.com

($\lambda = 1.5406$ Å) radiation. Scanning electron microscopy (SEM) analysis was carried out using a Hitachi SU 8000 instrument. High-resolution transmission electron microscope (HR-TEM) analysis was performed using a JEM-2100F instrument. X-ray photoelectron spectroscopy (XPS) spectra were acquired on a Thermo ESCALAB 250 spectrometer with Al $K\alpha$ irradiation at $\theta = 90°$ for X-ray sources, and the binding energies were calibrated using the C 1 s peak at 284.5 eV. FT-IR spectra were recorded using a Nicolet Impact 410 FTIR spectrometer. ^{13}C cross-polarization magic-angle spinning (CP-MAS) NMR measurements (100.5 MHz) were performed on a Varian infinity plus 400 spectrometer equipped with a magic-angle spin probe in a 4-mm ZrO_2 rotor. Gas adsorption isotherms were measured using a surface area analyzer ASAP 2020. The N_2 sorption isotherms were collected at 77 K utilizing a liquid N_2 bath. Grazing incidence wide-angle X-ray scattering (GIWAXS) measurements were conducted on a MicroMax-007HF instrument employing a high-intensity rotating anode X-ray generator, at an incident angle of 0.2°. The samples were recorded in the 2θ range of 2–40°, and the data were collected with Win software. 2D grazing incidence wide-angle X-ray scattering (2D-GIWAXS) was performed to analyze the orientation of the COF layer using an XEUSS SAXS/WAXS system at an incident angle of 0.2°. For 2D-GIWAXS, the membrane samples were cut into small pieces (1 × 1 cm) and attached to a silicon wafer. The 2D-GIWAXS data of the membranes were evaluated using a MarCDD X-ray detector. UV–Vis diffuse reflectance spectra were recorded using a SHIMADZU UV-2600 spectrometer.

Supporting Information

Supporting Information is available from the Wiley Online Library or from the author.

Acknowledgements

Conflict of Interest

The authors declare no conflict of interest.

Data Availability Statement

The data that support the findings of this study are available from the corresponding author upon reasonable request.

Keywords

[1] B. E. Logan, M. Elimelech, *Nature* **2012**, *488*, 313.
[2] Y. Zhou, L. Jiang, *Joule* **2020**, *4*, 2244.
[3] Y. Zhu, K. Zhan, X. Hou, *ACS Nano* **2018**, *12*, 908.
[4] Z. Zhang, L. Wen, L. Jiang, *Nat. Rev. Mater.* **2021**, *6*, 622.
[5] C. Chen, D. Liu, L. He, S. Qin, J. Wang, J. M. Razal, N. A. Kotov, W. Lei, *Joule* **2020**, *4*, 247.
[6] X. Zuo, C. Zhu, W. Xian, Q.-W. Meng, Q. Guo, X. Zhu, S. Wang, Y. Wang, S. Ma, Q. Sun, *Angew. Chem., Int. Ed.* **2022**, *61*, 202116910.
[7] S. Chen, C. Zhu, W. Xian, X. Liu, X. Liu, Q. Zhang, S. Ma, Q.i Sun, *J. Am. Chem. Soc.* **2021**, *143*, 9415.
[8] J. Hao, B. Bao, J. Zhou, Y. Cui, X. Chen, J. Zhou, Y. Zhou, L. Jiang, *Adv. Mater. 34*, **2022**, 2203109.
[9] H. Ling, W. Xin, Y. Qian, X. He, L. Yang, W. Chen, Y. Wu, H. Du, Y. Liu, X.-Y. Kong, L. Jiang, L. Wen, *Angew. Chem., Int. Ed.* **2023**, *62*, 202212120.
[10] Z. Zhang, P. Zhang, S. Yang, T. Zhang, M. Löffler, H. Shi, M. R. Lohe, X. Feng, *Proc. Natl. Acad. Sci. U.S.A.* **2020**, *117*, 13959.
[11] Y. Qian, D. Liu, G. Yang, L. Wang, Y. Liu, C. Chen, X. Wang, W. Lei, *J. Am. Chem. Soc.* **2022**, *144*, 13764.
[12] B. Cheng, Y. Zhong, Y. Qiu, S. Vaikuntanathan, J. Park, *J. Am. Chem. Soc.* **2023**, *145*, 5261.
[13] L. Cao, I.-C. Chen, C. Chen, D. B. Shinde, X. Liu, Z. Li, Z. Zhou, Y. Zhang, Y. Han, Z. Lai, *J. Am. Chem. Soc.* **2022**, *144*, 12400.
[14] J. Safaei, Y. Gao, M. Hosseinpour, X. Zhang, Y. Sun, X. Tang, Z. Zhang, S. Wang, X. Guo, Y. Wang, Z. Chen, D. Zhou, F. Kang, L. Jiang, G. Wang, *J. Am. Chem. Soc.* **2023**, *145*, 2669.
[15] Z. Zhang, P. Bhauriyal, H. Sahabudeen, Z. Wang, X. Liu, M. Hambsch, S. C. B. Mannsfeld, R. Dong, T. Heine, X. Feng, *Nat. Commun.* **2022**, *13*, 3935.
[16] J. Feng, M. Graf, K. Liu, D. Ovchinnikov, D. Dumcenco, M. Heiranian, V. Nandigana, N. R. Aluru, A. Kis, A. Radenovic, *Nature* **2016**, *536*, 197.
[17] J. Gao, X. Liu, Y. Jiang, L. Ding, L. Jiang, W. Guo, *Small* **2019**, *15*, 1804276.
[18] A. Siria, P. Poncharal, A.-L. Biance, R. Fulcrand, X. Blase, S. T. Purcell, L. Bocquet, *Nature* **2013**, *494*, 455.
[19] J. Yang, B. Tu, G. Zhang, P. Liu, K. Hu, J. Wang, Z. Yan, Z. Huang, M. Fang, J. Hou, Q. Fang, X. Qiu, L. Li, Z. Tang, *Nat. Nanotechnol.* **2022**, *17*, 622.
[20] L. Wang, Z. Wang, S. K. Patel, S. Lin, M. Elimelech, *ACS Nano* **2021**, *15*, 4093.
[21] J. Yang, B. Tu, M. Fang, L. Li, Z. Tang, *ACS Nano* **2022**, *16*, 13294.
[22] C. Zhu, X. Zuo, W. Xian, Q. Guo, Q.-W. Meng, S. Wang, S. Ma, Q. Sun, *ACS Energy Lett.* **2022**, *7*, 2937.
[23] W. Xian, X. Zuo, C. Zhu, Q. Guo, Q.-W. Meng, X. Zhu, S. Wang, S. Ma, Q. Sun, *Nat. Commun.* **2022**, *13*, 3386.
[24] K. Xiao, L. Jiang, M. Antonietti, *Joule* **2019**, *3*, 2364.
[25] R. Tan, A. Wang, R. Malpass-Evans, R. Williams, E. W. Zhao, T. Liu, C. Ye, X. Zhou, B. P. Darwich, Z. Fan, L. Turcani, E. Jackson, L. Chen, S. Y. Chong, T. Li, K. E. Jelfs, A. I. Cooper, N. P. Brandon, C. P. Grey, N. B. Mckeown, Q. Song, *Nat. Mater.* **2019**, *19*, 195.
[26] Y. Liu, Y. Chen, Y. Guo, X. Wang, X. Ding, X. Sun, H. Wang, Y. Zhu, L. Jiang, *ACS Nano* **2022**, *16*, 16343.
[27] T. Qian, H. Zhang, X. Li, J. Hou, C. Zhao, Q. Gu, H. Wang, *Angew. Chem., Int. Ed.* **2020**, *59*, 13051.
[28] R. Li, L. Zhang, L. Shi, P. Wang, *ACS Nano* **2017**, *11*, 3752.
[29] P. Liu, Y. Sun, C. Zhu, B. Niu, X. Huang, X.-Y. Kong, L. Jiang, L. Wen, *Nano Lett.* **2020**, *20*, 3593.
[30] Z. Zhang, X. Huang, Y. Qian, W. Chen, L. Wen, L. Jiang, *Adv. Mater.* **2020**, *32*, 1904351.
[31] Z.-Q. Li, G.-L. Zhu, R.-J. Mo, M.-Y. Wu, X.-L. Ding, L.-Q. Huang, Z.-Q. Wu, X.-H. Xia, *Angew. Chem., Int. Ed.* **2022**, *61*, 202202698.

[32] K. Xiao, P. Giusto, L. Wen, L. Jiang, M. Antonietti, *Angew. Chem., Int. Ed.* **2018**, *57*, 10123.

[33] P. Liu, T. Zhou, Y. Teng, L. Fu, Y. Hu, X. Lin, X.-Y. Kong, L. Jiang, L. Wen, *CCS Chem* **2020**, *2*, 1325.

[34] M. Graf, M. Lihter, D. Unuchek, A. Sarathy, J.-P. Leburton, A. Kis, A. Radenovic, *Joule* **2019**, *2*, 1549.

[35] T. Ding, G. W. Ho, *Joule* **2021**, *5*, 1639.

[36] D. Zhang, Y. Ren, X. Fan, J. Zhai, L. Jiang, *Nano Energy* **2020**, *76*, 105086.

[37] X. Xie, G. A. Crespo, G. Mistlberger, E. Bakker, *Nat. Chem.* **2014**, *6*, 202.

[38] K. Xiao, P. Giusto, F. Chen, R. Chen, T. Heil, S. Cao, L. Chen, F. Fan, L. Jiang, *Natl. Sci. Rev.* **2020**, *8*, nwaa231.

[39] K. Xiao, L. Chen, R. Chen, T. Heil, S. D. C. Lemus, F. Fan, L. Wen, L. Jiang, M. Antonietti, *Nat. Commun.* **2019**, *10*, 74.

[40] S. Yuan, X. Li, J. Zhu, G. Zhang, P. Van Puyvelde, B. Van Der Bruggen, *Chem. Soc. Rev.* **2019**, *48*, 2665.

[41] P. J. Waller, F. Gándara, O. M. Yaghi, *Acc. Chem. Res.* **2015**, *48*, 3053.

[42] C. Yin, Z. Li, D. Zhao, J. Yang, Y. Zhang, Y. Du, Y. Wang, *ACS Nano* **2022**, *16*, 14178.

[43] G. He, R. Zhang, Z. Jiang, *Acc. Mater. Res.* **2021**, *2*, 630.

[44] S. Kandambeth, D. B. Shinde, M. K. Panda, B. Lukose, T. Heine, R. Banerjee, *Angew. Chem., Int. Ed.* **2013**, *52*, 13052.

[45] G. Lin, H. Ding, R. Chen, Z. Peng, B. Wang, C. Wang, *J. Am. Chem. Soc.* **2017**, *139*, 8705.

[46] K. Liu, H. Qi, R. Dong, R. Shivhare, M. Addicoat, T. Zhang, H. Sahabudeen, T. Heine, S. Mannsfeld, U. Kaiser, Z. Zheng, X. Feng, *Nat. Chem.* **2019**, *11*, 994.

[47] Y. Qian, D. Li, Y. Han, H.-L. Jiang, *J. Am. Chem. Soc.* **2020**, *142*, 20763.

[48] X. Guo, T. Mao, Z. Wang, P. Cheng, Y. Chen, S. Ma, Z. Zhang, *ACS Cent. Sci.* **2020**, *6*, 787.

[49] J.-N. Chang, Q. Li, J.-W. Shi, M. Zhang, L. Zhang, S. Li, Y. Chen, S.-L. Li, Y.-Q. Lan, *Angew. Chem., Int. Ed.* **2022**, *62*, 202218868.

[50] X. He, Y. Yang, H. Wu, G. He, Z. Xu, Y. Kong, L. Cao, B. Shi, Z. Zhang, C. Tongsh, K. Jiao, K. Zhu, Z. Jiang, *Adv. Mater.* **2020**, *32*, 2001284.

[51] S. Bing, W. Xian, S. Chen, Y. Song, L. Hou, X. Liu, S. Ma, Q. Sun, L. Zhang, *Matter* **2021**, *4*, 2027.

[52] C. Yuan, X. Wu, R. Gao, X. Han, Y. Liu, Y. Long, Y. Cui, *J. Am. Chem. Soc.* **2019**, *141*, 20187.

[53] Y. Li, Q. Wu, X. Guo, M. Zhang, B. Chen, G. Wei, X. Li, X. Li, S. Li, L. Ma, *Nat. Commun.* **2020**, *11*, 599.

[54] F. Sheng, B. Wu, X. Li, T. Xu, M. A. Shehzad, X. Wang, L. Ge, H. Wang, T. Xu, *Adv. Mater.* **2021**, *33*, 2104404.

[55] Y. Ying, S. B. Peh, H. Yang, Z. Yang, D. Zhao, *Adv. Mater.* **2021**, *33*, 2104946.

[56] H. Fan, M. Peng, I. Strauss, A. Mundstock, H. Meng, J. Caro, *J. Am. Chem. Soc.* **2020**, *142*, 6872.

[57] L. Cao, X. Liu, D. B. Shinde, C. Chen, I.-C. Chen, Z. Li, Z. Zhou, Z. Yang, Y. Han, Z. Lai, *Angew. Chem., Int. Ed.* **2022**, *61*, 202113141.

[58] S. Zhao, C. Jiang, J. Fan, S. Hong, P. Mei, R. Yao, Y. Liu, S. Zhang, H. Li, H. Zhang, C. Sun, Z. Guo, P. Shao, Y. Zhu, J. Zhang, L. Guo, Y. Ma, J. Zhang, X. Feng, F. Wang, H. Wu, B. Wang, *Nat. Mater.* **2021**, *20*, 1551.

[59] L. Hou, W. Xian, S. Bing, Y. Song, Q. Sun, L. Zhang, S. Ma, *Adv. Funct. Mater.* **2021**, *31*, 2009970.

[60] Q. Sun, Y. Pan, X. Wang, H. Li, J. Farmakes, B. Aguila, Z. Yang, S. Ma, *Chem* **2019**, *5*, 3184.

[61] Q. Sun, B. Aguila, J. Perman, L. D. Earl, C. W. Abney, Y. Cheng, H. Wei, N. Nguyen, L. Wojtas, S. Ma, *J. Am. Chem. Soc.* **2017**, *139*, 2786.

[62] H. S. Sasmal, A. Halder, S. Kunjattu H, K. Dey, A. Nadol, T. G. Ajithkumar, P. Ravindra Bedadur, R. Banerjee, *J. Am. Chem. Soc.* **2019**, *141*, 20371.

[63] J. W. Colson, A. R. Woll, A. Mukherjee, M. P. Levendorf, E. L. Spitler, V. B. Shields, M. G. Spencer, J. Park, W. R. Dichtel, *Science* **2011**, *332*, 228.

[64] J. Liu, S. Wang, T. Huang, P. Manchanda, E. Abou-Hamad, S. P. Nunes, *Sci. Adv.* **2020**, *6*, eabb3188.

[65] C. Lee, A. Joly, A. Siria, A.-L. Biance, R. Fulcrand, L. Bocquet, *Nano Lett.* **2012**, *12*, 4037.

[66] C. Zhu, W. Xian, Y. Song, X. Zuo, Y. Wang, S. Ma, Q. Sun, *Adv. Funct. Mater.* **2022**, *32*, 2109210.

[67] M. J. Esplandiu, D. Reguera, D. Romero-Guzmán, A. M. Gallardo-Moreno, J. Fraxedas, *Nat. Commun.* **2022**, *13*, 2812.